Journal of Materials Science: Materials in Electronics (2019) 30:16761–16773
https://doi.org/10.1007/s10854-019-01289-x

Random laser materials: from ultrahigh efficiency to very low threshold (Anderson localization)

N. Wetter[1] · **E. Jimenez-Villar**[1,2]

Received: 24 January 2019 / Accepted: 5 April 2019 / Published online: 26 April 2019

Abstract
Random lasers hold the premise for cheap coherent light sources that can be miniaturized and molded into any shape and used for speckle-free imaging in biology, remote sensing, display technology, encrypting, cancer detection and distributed amplification. However, they require improvements specifically in terms of efficiency and low emission threshold. This work details for the first time a strategy for increasing the efficiency of a random laser that consists in using smaller particles, trapped between large particles to serve as absorption and gain centers whereas the large particles control mainly the light diffusion into the sample. A record slope efficiency of more than 50% was achieved using yttrium vanadate particles with mean particle size of 54 μm by optimizing the distribution of the polydispersed particles. In addition, random lasing with very low emission threshold (0.24 mJ/cm^2) is also reported in a strongly disordered optical medium that is in the transition regime to Anderson localization composed by a colloidal suspension of core–shell TiO_2@Silica nanoparticles in ethanol solution of rhodamine 6G. A promising method called fraction of absorbed pump power allowed us to infer the emission threshold for localized modes (peaks mode). The classical super-fluorescence band (ASE) of the random laser was measured separately by collecting the emission at the back of the samples, showing a linear dependence with pumping fluence without gain depletion. The intensity of peaks during Anderson transition is approximately equal within a broad frequency range, indicating suppression of the interaction between the peak modes. The random lasers have been characterized by measurements of backscattering cone, absorption and reflection measurement, transport mean free path, average photon path length and fill fractions.

1 Introduction

Random lasers (RLs) have been predicted in 1967 and experimentally verified for the first time in 1993 [1, 2]. RLs have been shown to work within a large number of different materials such as semiconductor nanoparticles, ceramic powders and polymers, organic materials and biological tissues [3–7]. However, in order to achieve useful output power for most real word applications, several issues of RLs have to be addressed. These are lack of directional output, high threshold and low efficiency. The lack of directionality has been addressed using one-dimensional (1-D) RLs such as fibers or 2-D RLs such as some DFB lasers [8, 9]. Recently, a 3-D RL has achieved an output beam with 68 mrad of divergence that corresponds to a typical beam quality of a solid-state laser with an M^2 of ten [10]. In order to decrease RL threshold, random lasing with distributed feedback was also addressed in a low dimensional system (optical fiber) [11]. However, an in-depth study in a 3-D RL is lacking. In this paper, we address solutions for increasing the efficiency and decreasing the threshold of 3-D RLs.

In the first part of this work, a strategy is described that managed to achieve, for the first time, a RL with more than 50% slope efficiency. This strategy uses three main ingredients: (1) choice of a highly efficient RL material, (2) concentration of the absorbed pump power into tiny volumes (called herein "pockets") that result in high gain regions and (3) optimization of the pump-to-laser overlap volume by pumping from all sides. Developers of bulk diode-pumped solid-state-lasers are well aware of these three ingredients and have pushed

✉ N. Wetter
nuwetter@ipen.br

✉ E. Jimenez-Villar
Ernesto.Jimenez@uv.es

[1] Centro de Lasers e Aplicações, Instituto de Pesquisas Energéticas e Nucleares CNEN-IPEN/SP, Av. Prof. Lineu Prestes 2242, São Paulo CEP 05508-000, Brazil

[2] Departamento de Física, Universidade Federal da Paraíba, João Pessoa, PB 58051-970, Brazil

Table 1 Groups of different grain size distributions for the monodispersed and polydispersed Nd^{3+}:YVO_4 powders measured by Fraunhofer laser diffraction technique

Mesh (μm)	Groups A—*polydispersed* Mean particle size		SD	Groups B—*monodispersed* Mean particle size		SD
10–20	A_1	9.5 μm	7.3	B_1	9.9 μm	0.98
20–45	A_2	15 μm	12	B_2	37 μm	2.17
45–75	A_3	30 μm	–	B_3	55 μm	–
75–106	A_4	54 μm	39	B_4	96 μm	4.7
106–180	A_5	125 μm	–	B_5	*147 μm	–

Measurement of group B5 was performed by SEM image analysis

efficiencies to well above 50% by optimizing them during the last two decades. In terms of materials for neodymium doped hosts, there has been a shift from the traditional $Y_3Al_5O_{12}$ (YAG) and $LiYF_4$ (YLF) crystals, to more efficient hosts, such as $GdVO_4$ and YVO_4, with larger emission cross-sections [12, 13]. The change from lamp-pumped technology to diode-pumping has caused not only a strong increase in spectral overlap between pump radiation and crystal absorption, increasing the overall efficiency from approximately 6% to more than 30% in the case of Nd:YAG lasers [14–16], but also a better spatial overlap between the pumped volume and the laser's mode volume. The spatial overlap is of paramount importance and was first exploited in longitudinally pumped laser designs and later was found to work just as well for side-pumped designs [17, 18]. The highest efficiencies reported so far for diode-pumped designs, operating at ambient temperatures, is in the range of 60% to 80% depending on laser material [13, 19]. Random Lasing of some of these materials has been shown before and characterized, but always with very small efficiencies, generally of the order of a few percent [20–22].

In the second part, another strategy for decreasing RL threshold is reported. A colloidal suspension of core–shell (TiO_2@Silica) nanoparticles (NPs) suspended in ethanol solution allowed us to observe the transition regime to Anderson localization [23–26]. It is well known that a scattering medium with gain, operating at the transition to Anderson localization, can sustain random lasing with coherent feedback [27], which could lead to a significant decrease of the RL threshold. In order to study random lasing in this critical regime, rhodamine 6G (R6G) was added to the TiO_2@Silica suspension. Narrow persistent peaks, with similar amplitude, overlapping on a super-fluorescence band were observed in the emission spectrum. The latter indicates a suppression of the interaction between these modes (narrow peaks), which represents a signature of random lasing at localization [28, 29]. This can be understood by realizing that the photons confined in a localized mode must be strongly correlated [30, 31]. Therefore, for different localized lasing modes, even with significant spatial or frequency overlap, the interactions between modes must be frozen above the RL threshold [28]. In a previous work [26], we interpreted the phase of localization transition as the coexistence of localized and extended modes due to the scattering strength inhomogeneity at the micrometric scale, which can be a consequence of the correlation in the particle positions. This latter would be originated by the long-range interaction between TiO_2@Silica NPs ($\geq$ mean spacing) by the repulsive electric force, which depends strongly on the NPs size and the dielectric constant of the solution (ethanol). Thereby, the colloid cannot be addressed as an ideal gas, i.e. the NP positions and their spacing distribution would cease to be random, which induces an inhomogeneity in the NP concentration and a certain order at the microscopic scale. The inhomogeneous distribution of scatterer positions at the microscopic scale should lead to micrometric regions with kl_T values lower than the averaged kl_T value determined experimentally.

2 Sample preparation and laser set-up

2.1 First part (poly-dispersed Nd^{3+}:YVO_4 powder)

Milling of the yttrium vanadate crystal powder, doped with 1.33 mol% of neodymium (Nd^{3+}:YVO_4) was done using a mortar and pestle of agate. Different sizes of sieves, ranging from 10 μm mesh to 180 μm mesh, were used to obtain different particle sizes. A stainless-steel mold was specially developed and adapted to a mechanical press for different compaction pressures to be studied. Table 1 shows the different grain sizes obtained. The samples were produced in disk form of 7 mm in diameter, approximately half of a millimeter thick and with 60 mg of powder. Each sample was reproduced three times [32].

Polydispersed samples were obtained by just collecting the powder in each sieve. These samples had a large fraction of smaller particles sticking to the bigger grains. In order to achieve the monodispersed samples, an extra cleansing procedure was developed which basically involved washing the powders with isopropyl alcohol in ultrasound and sieving again. Size measurements by the Fraunhofer diffraction technique include the solvation layer. However, this layer has only tens of nanometers thickness and therefore is negligible.

After compacting the powders into pellets, the samples were mounted on a slowly (20 Hz) rotating sample holder and

irradiated by means of a 105 W, quasi-continuous wave laser diode emitting at 805 nm. The simple set-up consisted of the diode laser followed by beam shaping optics, a beam splitter to separate the 805 nm pump radiation going to the sample from the returning 1064 nm random laser radiation and a f = 20 mm spherical lens for focusing onto a spot of 3 mm^2 size at the samples. An energy sensor was positioned behind the beam splitter and captured the random laser radiation.

2.1.1 Pressure optimization

In the first laser experiment we optimized in terms of laser efficiency the applied pressure used for compacting the pellets. Upon increasing the pressure from 50 to 250 MN/m^2 to mold the pellets, the powder grains get closer together and an increase in scattering density of light is expected. However, at still higher pressure we observed an increasingly higher density of fractures in the larger grains and also, the surface of the pellets showed increasingly voids where smaller particles were lost (Fig. 1).

Using the laser pump-setup described above we experimented with pellets from group A4 using pressures of 51 MN/m^2, 219 MN/m^2, 255 MN/m^2, 297 MN/m^2 and 510 MN/m^2. The results are shown in Fig. 2a. We also verified if the other groups would show the same results as a function of pressure and all groups showed the best results for 255 MN/m^2. However, the optimum pressure depends very strongly on how this pressure is applied. We wondered what would happen if we applied the same pressure not once but twice: one first time with half of the material used for a pellet (30 mg) and a second time with all of the material. The motive for this research was that due to the strongly randomized shape of the crystallites, the compaction in the center of the pellet should be less than on the surface, causing an inhomogeneous particle density and fill fraction as a function of pellet depth. To our surprise the effect of this two-step compaction process was a very large difference in efficiency as shown in Fig. 2b. For the rest of the experiments all samples were compacted in a single step for simplicity although there is a chance that samples with a more homogenous particle density, obtained by several steps of compaction, could give better overall results.

2.1.2 FAP measurements

A very important measurement that gives detailed insight into what happens within the samples is the measurement of the fraction of absorbed pump power (FAP, Eq. 1). It allows

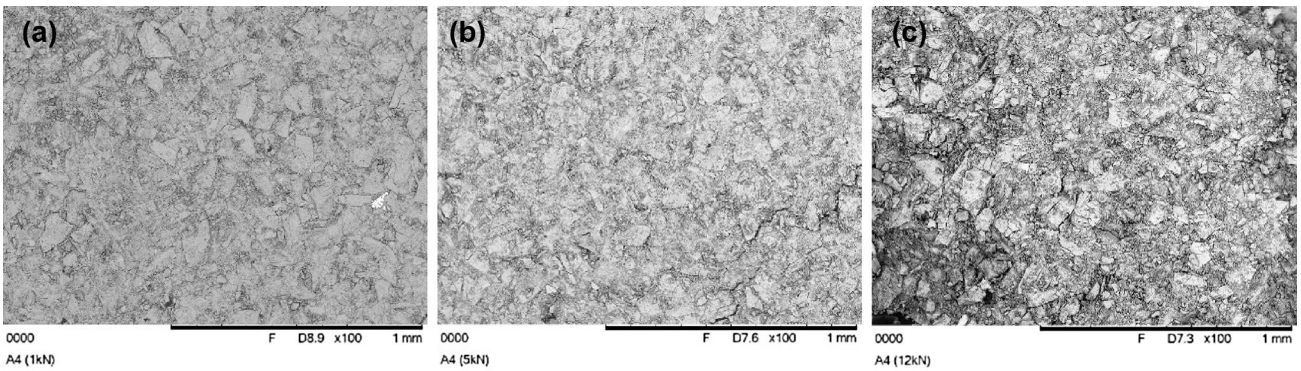

Fig. 1 SEM images of pellet surfaces from group A4, compacted at different pressures. **a** 51 MN/m^2, **b** 255 MN/m^2 and **c** 612 MN/m^2

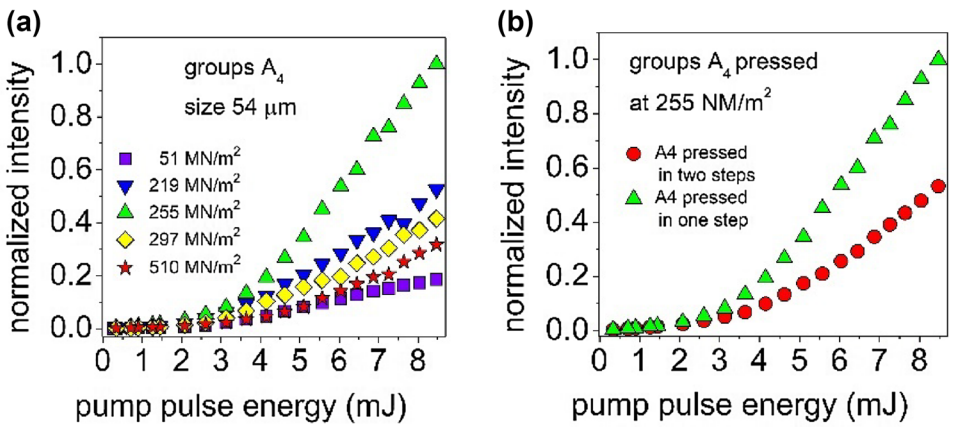

Fig. 2 **a** Normalized output power at 1064 nm of the RL samples of group A4 as a function of pump power and pressure applied to compact the pellet. Best experimentally verified pressure is 255 NM/m^2. **b** Two-step compaction of pellet causes an almost 50% decrease in efficiency

for calculation of the average photon path length within the sample (l_c), which, when divided by the transport mean free path (l_t), gives the average number of scattering events. An increase in scattering events is directly linked to an increase in the probability that a photon gets absorbed (Eq. 2).

The FAP measurement compares the intensities reflected from the samples with (I_{R+A}) and without absorption (I_R) from the laser active ion.

$$FAP = \frac{I_R}{I_{R+A}} \approx \frac{I_{705\ \mathrm{nm}}}{I_{805\ \mathrm{nm}} e^{-l_c/l_a}} = e^{l_c/l_a}$$
$$\Rightarrow \ln(FAP) \approx {}^{l_c}/_{l_a} \rightarrow l_c \approx l_a \times \ln(FAP) \quad (1)$$

In the case of traditional random lasers, that use scattering centers and some laser active dye such as rhodamine in ethanol solution, this is achieved by measuring the reflected intensity at the same wavelength with and without rhodamine. In our case, where we do not have separate samples doped with and without neodymium, we use two nearby wavelengths, one at the neodymium absorption peak (805 nm) and one at a wavelength without absorption by neodymium (705 nm) under the assumption that the dispersion properties of the samples do not change significantly between these two wavelengths.

The absorption measurements were carried out with an integrating sphere operating in the specular included mode (Agilent, model Cary 5000). The integrating sphere was calibrated using test samples with known reflection; a diffusive Spectralon sample provided by the equipment manufacturer and a mirror with known reflection curve from Layertec GmbH. Then a first measurement was carried out at 705 nm (zero absorption) and a second measurement at 805 nm (absorption peak). Care was taken to tune the spectrometer always to the peak absorption to within 0.2 nm. For each group a measurement of three samples was performed by two different operators and the mean value was determined.

One important correction is the subtraction of the first surface reflection (sample surface) from the measured values. When observing the surfaces of the samples (Fig. 1), it is clearly seen that the bigger the particles, the more precisely they align perpendicular to the pressure applied during preparation of the pellets, thereby reflecting more light. Also, the larger the average grain size, the higher the probability that there are large voids between the big particles, decreasing thereby reflection. This behavior can be observed in Fig. 3a (705 nm curve). We also tried to measure the group's differences in first surface reflection by measuring the differences in values of specular included and excluded with the integrating sphere but the results were inconclusive. We therefore used an average surface reflection of 11%, corresponding to an index of refraction of 2.03, in all samples.

Figure 3b shows the results of the FAP measurements. A higher fraction of absorbed pump power is clearly observed for the polydispersed groups.

2.1.3 Determining the fill fraction and photon path length

Absorption within the samples is a function of the fill fraction, *ff*, and the transport mean free path, l_t. The macroscopic absorption length of Eq. (1) is the ballistic absorption length l_a (256 µm; [32]) divided by the fill fraction. The microscopic absorption length is therefore given by:

$$l_{abs} = \sqrt{\frac{l_t l_a}{3ff}} \quad (2)$$

One way to calculate the fill fraction is by experimentally determining l_t by measuring the backscattering cone (BSC) and compare these results with calculations of l_t using the histograms of the particle size distribution [33, 34]. The experimental measurements return the transport mean free path within the physical sample whereas the calculations

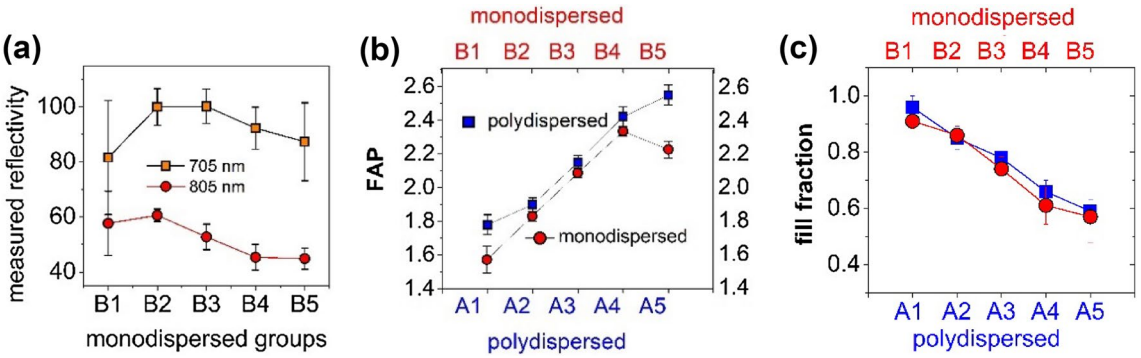

Fig. 3 **a** Reflectivity measurements (specular included) of the monodispersed groups before correction for surface reflectivity at wavelength of maximum (805 nm) and minimum (705 nm) absorption. **b** Resulting FAP values for polydispersed groups (squares) and monodispersed groups (circles). **c** Fill fraction calculated for the monodispersed groups (circles) and polydispersed groups (squares)

return l_t of a sample with fill fraction equal to one. The ratio of both results gives the actual fill fraction. The method used to calculate the histograms is based on the Fraunhofer laser diffraction technique that gives good results for particles in the range of 1 µm to 100 µm. Therefore, we had to employ additional techniques in order to calculate the histograms of A1, A2 and B1 that contained a lot of particles of less than 1 µm diameter [32].

As can be observed in Fig. 3c, the fill fraction decreases with mean particle size because for larger average particle size less smaller particles are available to fill the voids as the surface to volume ratio decreases and the smaller particles tend to stick to the surface of the larger particles. Also, the monodispersed groups have on average a smaller fill fraction because of the additional cleansing procedure used precisely to remove part of the smaller particles. From Fig. 3c one obtains that, on average, groups A have a 2% higher fill fraction than groups B. However, it should be pointed out that these are volume fractions and therefore, the number of smaller particles in groups A can be much higher than in group B. For example, the average particle size of the smallest particles that occupy 10% volume fraction in group A4 is 6 µm whereas in group B4 it is 31 µm.

We may now use Eq. (1) to calculate the average photon pass length within the sample and the number of scattering events.

As may be observed in Fig. 4a, the mean photon path length is approximately the same for both groups. This is an important result once it clearly states that light dispersion within the samples on a macroscopic level is governed by the large particles which are common to both groups.

As explained above, measurements of the transport mean free path were achieved by BSC and size distribution histograms. For all groups l_t ranged from 2 µm to 5 µm with the smaller particle groups showing the lower l_t values. The additional cleansing procedure, used to decrease the number of smaller particles within the monodispersed samples, was visually more effective for groups B3 to B5 whereas groups B1 and B2 still contained a large number of smaller particles (see Fig. 5a). This resulted in similar l_t values for A1 and B1 and A2 and B2 (Fig. 4b). Large differences in l_t values were observed for A and B groups three, four and five, as shown, with the smaller values of l_t belong to the polydispersed groups. Groups with very large average size of particles, such as A5 and B5, showed both very few smaller particles and therefore the difference in l_t decreases again.

The largest difference in transport mean free path of 15% is observed for groups 4. If we consider that l_C is approximately the same for both groups then group A4 has on average 15% more scattering events than group B4. These scattering events must occur within the pockets containing smaller particles which are responsible for only a 2% increase in volume fraction as we have seen before. In other words, the absorbed energy density within is approximately five times higher than outside of the pockets. This should cause a smaller laser threshold as well as a higher slope efficiency. Therefore, the pockets may be considered as gain centers of the random laser.

2.2 Second part (TiO_2@Silica NPs suspension in R6G solution)

Ethanol of high purity for liquid chromatography with spectroscopic grade purity was supplied by MERCK, tetra-ethyl-ortho-silicate (TEOS) was supplied by Sigma-Aldrich, and the ammonia pro analysis was also supplied by MERCK. The TiO_2 with a rutile crystal structure was acquired from DuPont Inc. (R900). The TiO_2 grains have an average particle diameter of 410 nm with a polydispersity of 25%. TiO_2 NPs were coated with a silica shell of ~40 nm thickness via the Stöber method [35]. In the first stage, 5 g of TiO_2 NPs was dispersed in 500 mL of ethanol. This suspension was placed in an ultrasound bath for 20 min to disperse the particles, and 6.67 mL of ammonia and 10 mL of TEOS were added. The TEOS and commercial ammonia (NH_4OH

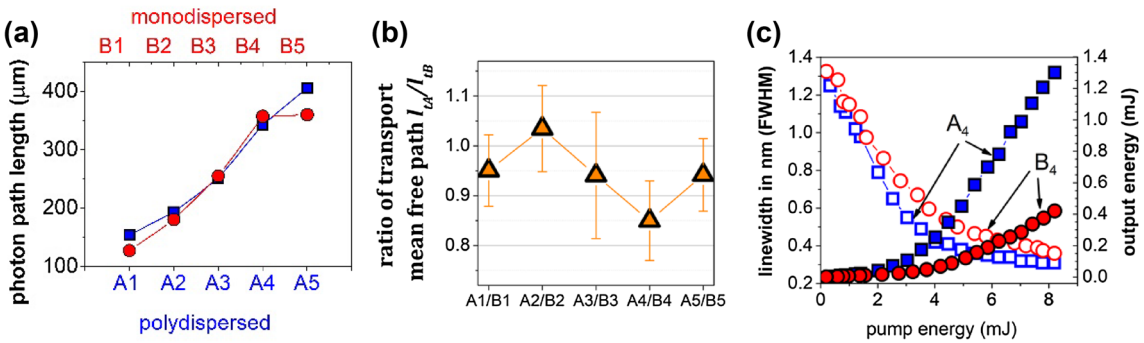

Fig. 4 **a** Mean photon path length within the samples for both groups. **b** Ratio of transport mean free path of polydispersed and monodispersed groups. **c** Comparison of output power and linewidth narrowing for groups A4 and B4

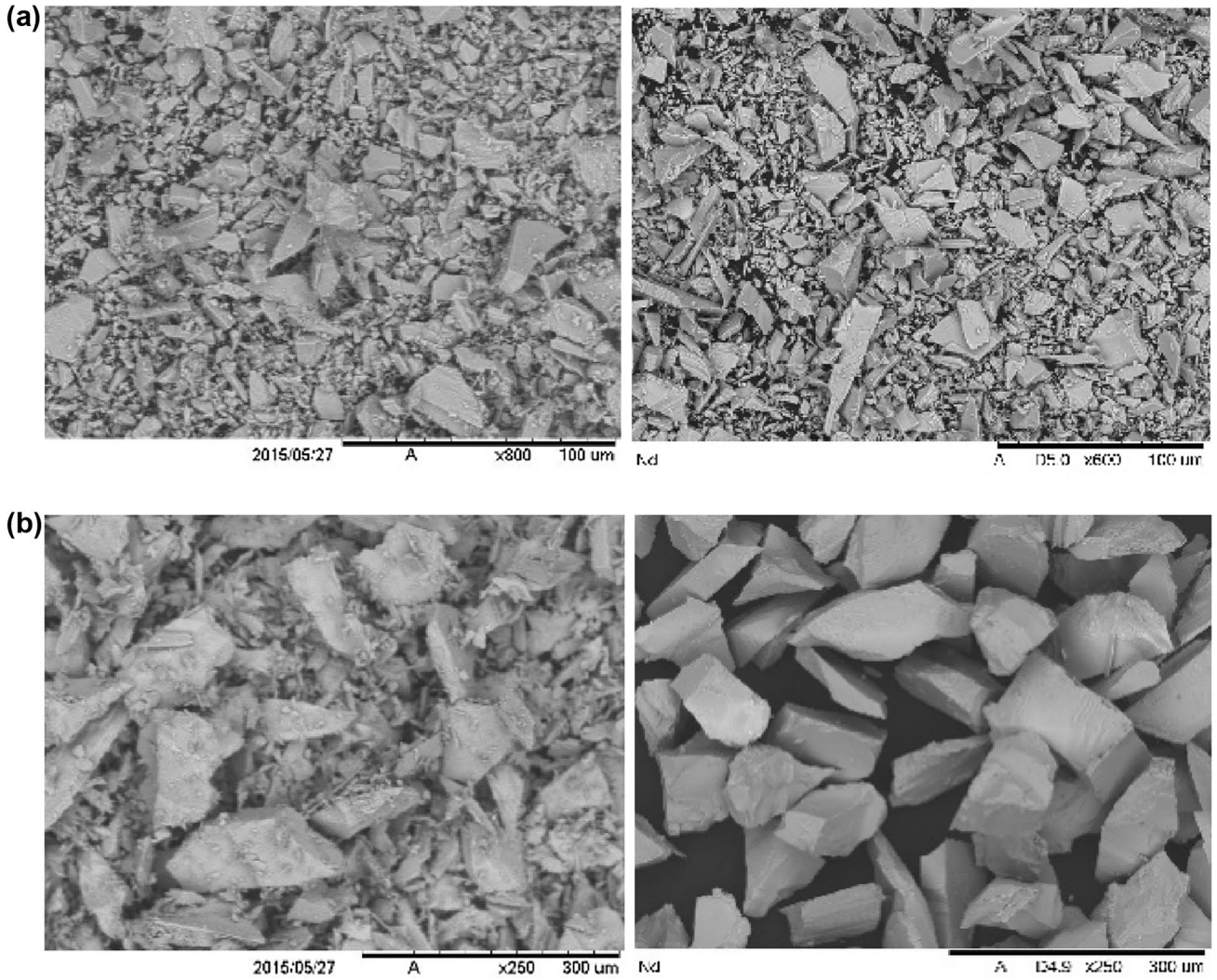

Fig. 5 **a** Comparison of power samples A1 with B1. Scale is 100 µm. **b** Comparison of A4 with B4. Scale is 300 µm

28–30%) were added alternately in 100 portions of 100 and 220 µL, respectively. The silica coating with thicknesses around or above 40 nm prevents the "optical" junction of the TiO_2 scattering surfaces (steric "optical" effect). We called this property optical colloidal stability [36]. Additionally, the silica shell provides a light–coupling enhancement with TiO_2 scattering cores [37], inertness [38–41], and high dispersibility [42–45], which has enabled their use in numerous applications [46–48]. The synthesized TiO_2@Silica NP suspension was rota-evaporated, dried in an oven at 70 °C for 2 h, and re-dispersed in ethanol at 140×10^{10} NPs mL^{-1}, equivalent to a filling fraction of ~ 10.6%. The ζ-potential value of the core–shell TiO_2@Silica NPs dispersed in ethanol, calculated from the electrophoretic mobility using the Henry´s approximation [49], was − 75 mV, which implies in appreciable and long–range repulsive forces between scatterers. R6G at [1×10^{-4} M] was added to the ethanol solution containing TiO_2@Silica NPs at [140×10^{10} NPs mL^{-1}]. The transport mean free path (l_T) for this [NPs], determined in previous work [23], is $l_T = 1.3$ µm.

2.2.1 Random laser action

Figure 6 shows typical RL emission spectra and the behavior of the spectral width [full width at half-maximum (FWHM)]. Schematic diagrams of the experimental setups used for this RL studies (frontal collection) can be found in our previous work [7]. Typical emission spectra of the RL below (0.1 mJ/cm^2), close (1.2 mJ/cm^2), above (12 mJ/cm^2) and well above (60 mJ/cm^2) the RL's threshold are shown in Fig. 6a–d, respectively. The RL emission spectra show intensity increase and bandwidth narrowing when the pumping energy fluence is increased. The emission intensity increases around 3 orders for pumping fluencies from 0.1 to 60 mJ/cm^2 (below and well above the RL threshold, respectively). Figure 6e shows the behavior of the spectral

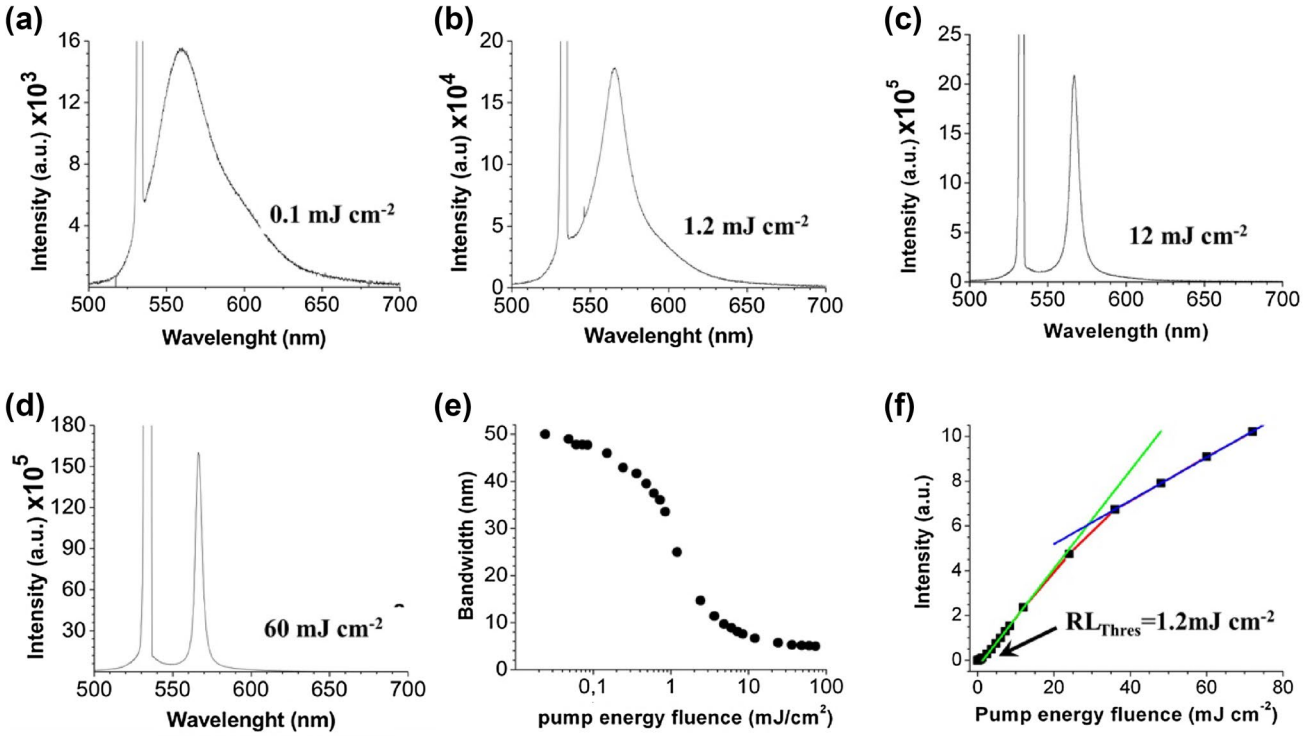

Fig. 6 Typical emission spectra of the RL for three pumping energy fluencies: **a** below (0.1 mJ/cm^2), **b** around (1.2 mJ/cm^2), **c** above (12 mJ/cm^2) and **d** well above (60 mJ/cm^2) the RL threshold. **e**–**f** Influence of the pump energy fluence on **e** RL spectral width (FWHM) and **f** RL emission intensity showing the RL threshold (RL_{thres}) (Color figure online)

width (FWHM), as a function of the pump energy fluence. A typical bandwidth narrowing is observed when the pump fluence increases (from ~ 50 nm down to ~ 5 nm). Figure 6f shows the behavior of the emitted intensity as a function of pump energy fluence. The RL slope efficiency (RL_{eff}) is not constant; it decreases markedly for pump fluencies from 12 up to 36 mJ/cm^2, showing a saturation of the emission. The green line represents the RL_{eff} for fluencies < 12 mJ/cm^2. For pumping fluencies ≥ 36 mJ/cm^2, RL_{eff} adopts a 2.3 times smaller value (blue line). The RL threshold (~ 1.2 mJ/cm^2) was determined by extrapolating the straight line corresponding to RL_{eff} (green line) to zero emission intensity.

2.2.2 Micrometric collection

Owing to the density of localized states at the sample's surface, localization should increase in the vicinity of the sample boundary [50, 51], a study has been performed collecting RL emissions from a micrometric region (~ 3.8 µm diameter) near the input-pump surface (less than 4 µm depth) using a detection system that performs like a confocal microscope. The experimental setup is shown in Fig. 7a. The light of the pump pulse reflected by the samples was measured with and without R6G. We designated the ratio between the pump intensities reflected by the scattering medium with and without R6G as the fraction of absorbed pumping (FAP), which represents the absorbance of the sample, ln(FAP) [36]. The FAP values from the small micrometric volume ($FAP_{(\mu m)}$) were measured with the same experimental setup. The $FAP_{(\mu m)}$ values for fluencies < 0.036 mJ/cm^2, well below the laser threshold ($FAP_{bT(\mu m)}$), are constant (~ 1.47), which represents a passive regime. For fluencies between 0.036 and 0.24 mJ/cm^2, the $FAP_{(\mu m)}$ value decreases quickly down to ~ 1.24, where it remains approximately constant up to a fluence of ~ 2.4 mJ/cm^2. The latter implies that for this range of fluencies (0.24–2.4 mJ/cm^2), a stationary regime is reached in this micrometric volume near the input-pump surface (< 4 µm depth), indicating that RL threshold in this micrometric region near the input border is around 0.24 mJ/cm^2. The $FAP_{(\mu m)}$ value starts to drop again quickly for fluencies > 8.6 mJ/cm^2 and decrease down to ~ 1 (null absorbance) for fluencies ≥ 36 mJ/cm^2. This means that absorbance in this micrometric volume (near the input-pumping surface) becomes practically zero for fluencies ≥ 36 mJ/cm^2. The emission spectra were acquired by integrating 21 laser shots. For an appropriate signal-to-noise ratio, an integrating time of 1.4 s at a repetition rate of 15 Hz was required. At the pump fluence of 9.6 mJ cm^{-2}, the emission spectra integrated from 6 laser shots were also

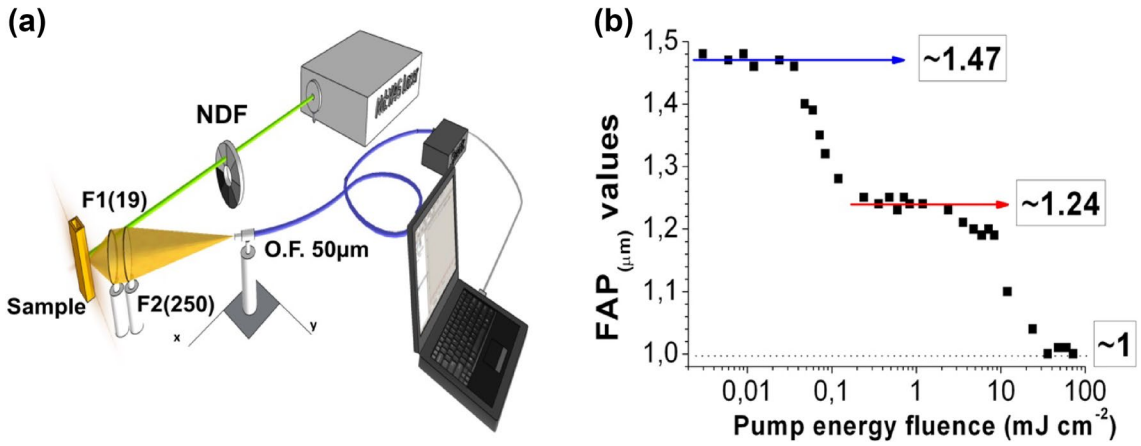

Fig. 7 **a** Schematic diagram of the experimental setup used for measurements of RL action and $FAP_{(\mu m)}$ in a small micrometric volume near to the input interface (< 4 µm depth); NDF is a neutral density filter; an optical fiber of 50 µm is used to collect the RL emission, F_1 (19) and F_2 (250) are lenses with focal lengths of 19 mm and 250 mm, respectively. The lenses diameters are one inch. The diameter of the collection volume is estimated in < 4 µm. The diameter of the pump spot is 3 mm. **b** FAP from the micrometric volume ($FAP_{(\mu m)}$), as a function of the pump energy fluence. $FAP_{(\mu m)} \approx 1$ for pump fluencies ≥ 36 mJ/cm^2

recorded for comparison, obtaining a good signal-to-noise ratio. However, for higher pumping intensity, the amount of narrow peaks did increase and their intensity did saturate, provoking a decrease in definition of these peaks.

Figure 8a and b show the RL emission spectra for a pump intensity of 9.6 mJ cm^{-2}, integrating 21 and six laser shots, respectively. Figure 8c–f show the RL emission spectra for a pump fluence of 6 mJ cm^{-2}, integrating 21 laser shots and collecting them with a delay of ~ (10–20) seconds between each. The frequency of these sharp peaks changes little in a few seconds, it only changes completely after tens of seconds or by stirring the sample. The RL is a liquid suspension, which means a continuous change in the particle configuration. In this way, if peaks of the emission spectrum

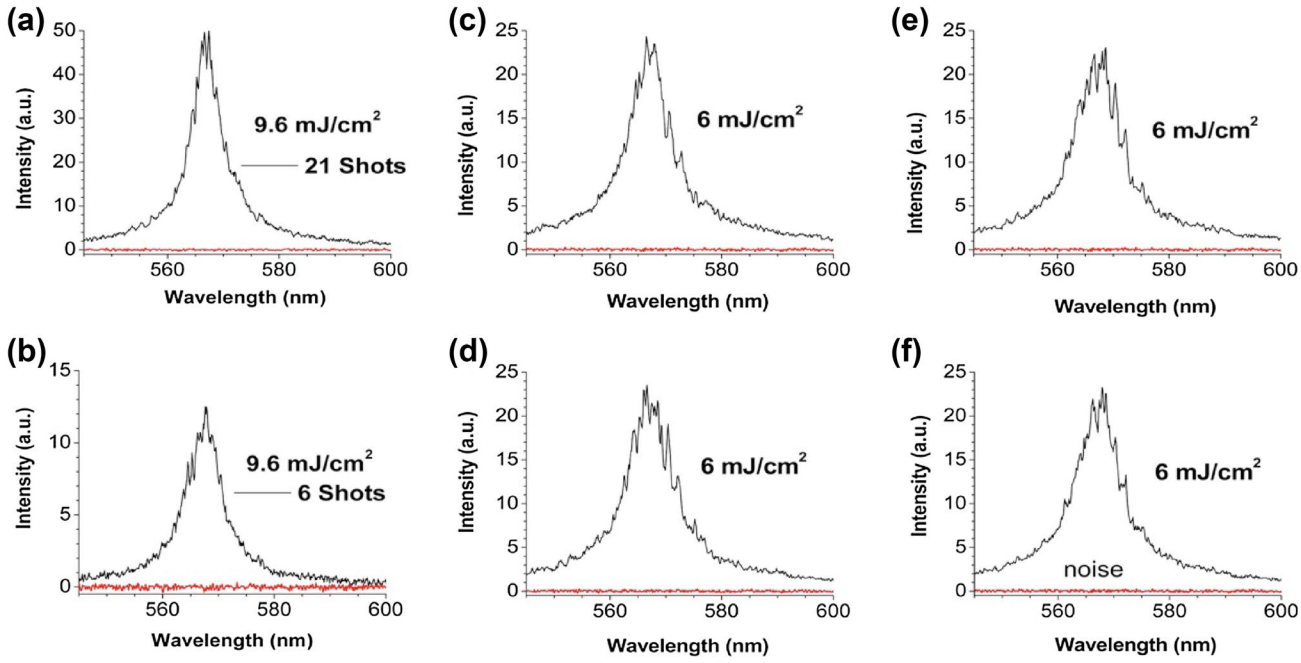

Fig. 8 Emission spectra collected from a small micrometric volume (< 4 µm diameter) near the input interface (< 4 µm depth) for pumping fluencies of: 9.6 mJ cm^{-2}, integrating **a** 21 and **b** 6 laser shots; **c**–**f** 6 mJ cm^{-2}, integrating 21 laser shots, and collected with a delay of ~ (10–20 s) between each spectrum. The solid red lines represent the respective noise signals (Color figure online)

are depending on particle configuration, these peaks should change after some time or by stirring the sample, like it was observed. We point out that the intensity of these narrow peaks, relative to the fluorescence band, is lower than that reported by Cao et al. [52], which could be a consequence of the extremely reduced (effective) size of their random laser. ZnO nanoparticles of 50 nm clustered in micrometric structures (diameter of several micrometers) compose their random laser. In turn, it is known that the density of strongly localized modes (anomalous localized modes, long lifetime) increases in the vicinity of the boundary, which was theoretically predicted by Mirlin in disordered electronic media [50, 51]. The anomalous localized modes are those where the boundary is part of the closed loop path (localized state). Thereby, the density of anomalous localized modes (long lifetime) must increase and the total amount of localized modes decreases as system size is decreased below localization length. The latter can be interpreted as an increase in the extent of localization (modes of long lifetime, decrease of the effective localization length) for a reduced number of anomalous localized modes (decrease of the total amount of localized modes) within these micrometric clusters [50, 51]. Additionally, an increase of the effective refractive index is expected near the boundaries due to the localization [23, 26, 53]. Consequently, owing to the fact that surface-volume ratio is considerably higher in these clusters; the interference (localization) must be increased, since the photon pathlength is forced to be longer due to the internal reflection. The latter can be understood such that the presence of a finite barrier in the border provokes an increase of the quantum interference (localization), which was theoretically demonstrated by Ramos et al. in disordered electronic media [54] and experimentally by us in this TiO_2@Silica colloidal suspension [26]. Therefore, lasing emission in their sample (clusters) must be confined to fewer lasing modes (anomalous localized modes) with higher intensity (high quality factor, long lifetime). However, our sample is a three-dimensional (3D) semi-infinite system with just one effective border, the input interface (silica-sample). On the other hand, contrary to our sample, where an R6G quantum efficiency near unity is expected, the fluorescence in their sample must be greatly quenched due to the superficial defects and dangling bonds of ZnO nanoparticles. Nevertheless, the excitation of ZnO or R6G molecules within the closed loop paths (excitation within localized state) would be free of quenching, since such molecules would be strongly correlated [30, 31]. Therefore, the intensity ratio (peaks/fluorescence) reported in ref. 53 (clusters) must be necessarily greater than that observed in our sample. In this way, the system studied in ref. 53 (very small size) should be addressed as a particular case of random lasing at localization or localization transition in 3D (reduced size). Indeed, in a subsequent study conducted by the same group [55], ZnO spheres of 85–617 nm diameters were cold pressed to form pellets. In this case, the relative intensity of the sharp peaks was considerably lower and for the sample of 85 nm spheres, lasing was not observed, which was attributed to a drastic increase of the random laser's cavity size brought about by an increase in transport mean free path. The latter indicates that the clustered structure (composed by 50 nm NPs) with very small dimensions (micrometric) [52] must play a crucial role in the localized lasing phenomenon. The above perspective represents another approach to addressing random lasing in localization, since the shape and size of a random laser should have strong influence on localization and consequently on random lasing.

2.2.3 Back collection

From the above results can be inferred that RL emission is composed by two completely different modes, the superfluorescence band (extended mode or ASE), and the narrow peaks (peaks mode). To determine the contribution of both RL modes, an additional experiment was designed. Let us introduce the following conjecture: if the narrow peaks are derived from localized modes due to the localization phenomenon, then they should basically be backscattered, that is, their emission should be detected in the direction opposite to the pump direction. Note that the emission of localized modes inside the sample is exponentially attenuated, so that if they are very near the front edge, they will be detected only in the spectrum obtained from the front surface (frontal spectrum) because they are too far from the back edge to survive, as the attenuation is huge. Thereby, the RL emission was also collected from the back of the cuvette (back collection). A schematic diagram of the experimental setup for the studies of RL back-collected emission is shown in Fig. 9a. An optical fiber of 200 μm was placed near to the back surface of a quartz cuvette, in order to collect the RL emission after it traversed the sample. The collected spectra consisted of a broad emission band (~ 50 nm bandwidth) with an overlapped single emission band, whose intensity and bandwidth are dependent of the pumping energy (Fig. 9b–e). In order to determine the RL emission band, two methods were used: (1) the previously rescaled fluorescence spectrum at a fluence < 0.5 mJ cm^{-2} was reduced to the collected spectra, (2) the emission spectrum was deconvoluted with several Gaussians, extracting a baseline that allows also to determine the superimposed emission band of the random laser. The results of both methods are similar. Figure 9b–e show the spectra collected at the back of the cuvette. Figure 9f shows the bandwidth of the emission spectrum, extracted from the frontal and back collection, as a function of the pumping energy fluence. As can be observed, the bandwidths of the frontal-spectra are larger than the back-spectra. Additionally, the frontal spectra are slightly asymmetrical, showing

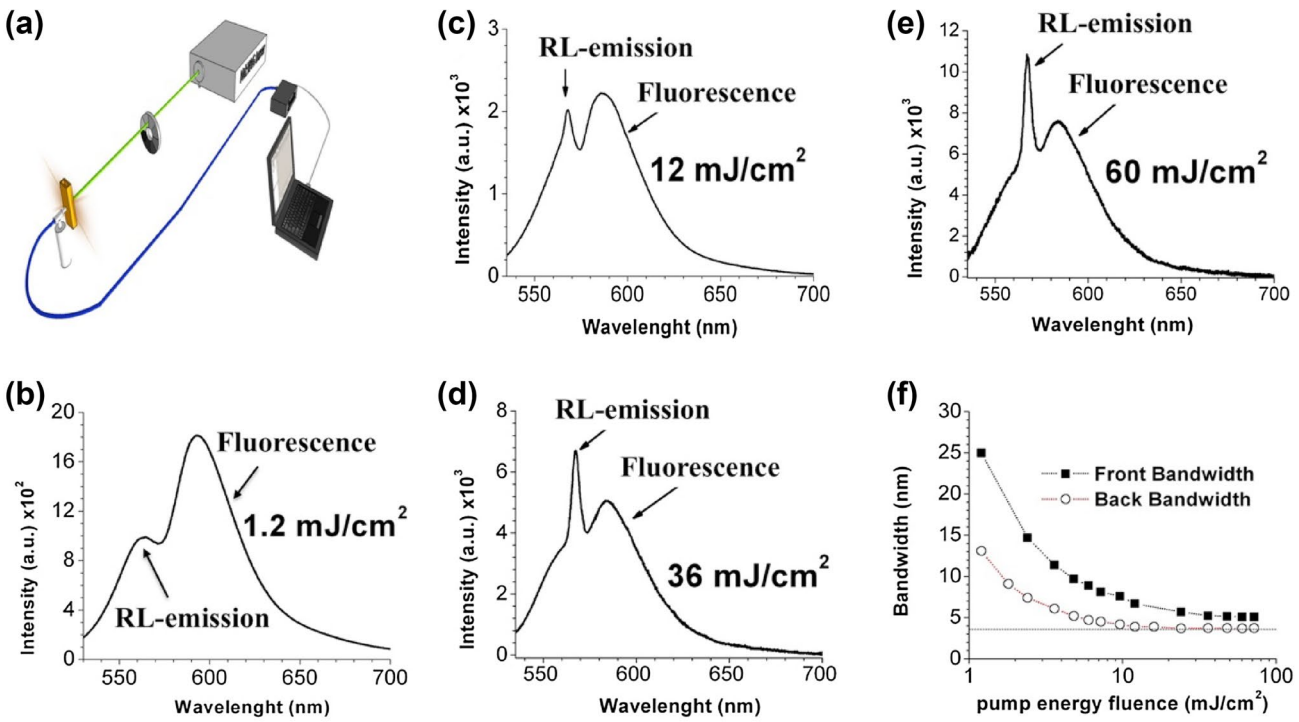

Fig. 9 **a** Schematic diagram of the experimental setup for back collection of RL emission. RL emission spectra by this back-collection method for pumping fluencies of: **b** 1.2 mJ cm^{-2}, **c** 12 mJ cm^{-2}, **d** 36 mJ cm^{-2}, and **e** 60 mJ cm^{-2}. The arrows denote the RL emission and R6G fluorescence band, respectively. **f** Bandwidth of the emission spectrum, extracted from the front and back collection, as a function of the pumping energy fluence

a widening towards longer wavelength (Fig. 10). Figure 10 shows the emission spectra from the frontal collection, the back collection and the subtraction between both spectra (front-back), for fluencies of 12 mJ cm^{-2}, 36 mJ cm^{-2} and 60 mJ cm^{-2}. The resulting spectrum from the subtraction between both spectra, which must correspond to the peaks' emission spectrum integrated over the whole emission volume, shows a plateau of intensity of approximately 2 nm to 3 nm. This indicates suppression of interaction between the peaks, which is a signature of random lasing at localization.

The intensity of the emission spectrum was plotted as a function of the pump energy fluence (Fig. 10a, Back RL). The experimental points were rescaled such that, $RL_{eff\text{-}back}$ was equal to the saturated RL_{eff} obtained for frontal collection (Fig. 6f, fluencies > 36 mJ cm^{-2}, blue line). The RL emitted light should traverse through the sample and, as a result, will suffer attenuation. If we consider that the saturated RL_{eff} (Fig. 6f, fluencies > 36 mJ cm^{-2}, blue line) corresponds to the RL_{eff} of the band mode (ASE; $RL_{eff\text{-}B}$), because the RL peaks mode is saturated, we can rescale the experimental points by a factor such that the $RL_{eff\text{-}back} = RL_{eff\text{-}B}$. The $RL_{eff\text{-}back}$ was constant without depletion (Fig. 10a, magenta line). The RL threshold for the band mode, determined from extrapolating $RL_{eff\text{-}back}$ to zero, is ~ 4 mJ/cm^2. The latter explains why RL threshold for frontal-collection (1.2 mJ/cm^2) is higher than that inferred from $FAP_{(\mu m)}$ (0.24 mJ/cm^2) in micrometric collection. Note that frontal emission is an overlapping of both modes (peaks and band modes). Figure 10b shows the behavior of the spectrally integrated RL emission for the frontal integrated collection (collected over the whole emission volume) and back collection (in exact analogy to Fig. 10a where we analyzed the peak spectral intensity instead). From the relationship between RL efficiencies < 8.4 mJ/cm^2 and > 36 mJ/cm^2, we can infer that for < 8.4 mJ/cm^2, ~ 74% of the RL emission, detected with our experimental setup, corresponds to the peak modes. Thereby, a simple calculus confirms that the RL threshold for the peak modes is effectively 0.24 mJ/cm^2. Note that the averaged value of the RL threshold (peaks and band modes) can be expressed as:

$$RL_{Thres-peak} \times 0.74\% + RL_{Thres-band} \times 0.26\%$$
$$\cong 1.2\frac{mJ}{cm^2} \Rightarrow RL_{Thres-peak}$$
$$\cong \frac{4 \times 0.26}{0.74} \cong 0.24\ \mathrm{mJ/cm^2}$$

This indicates that the RL threshold for localized modes is considerably lower than that for band or ASE mode. In this way, RL lasing at the critical regime of localization opens

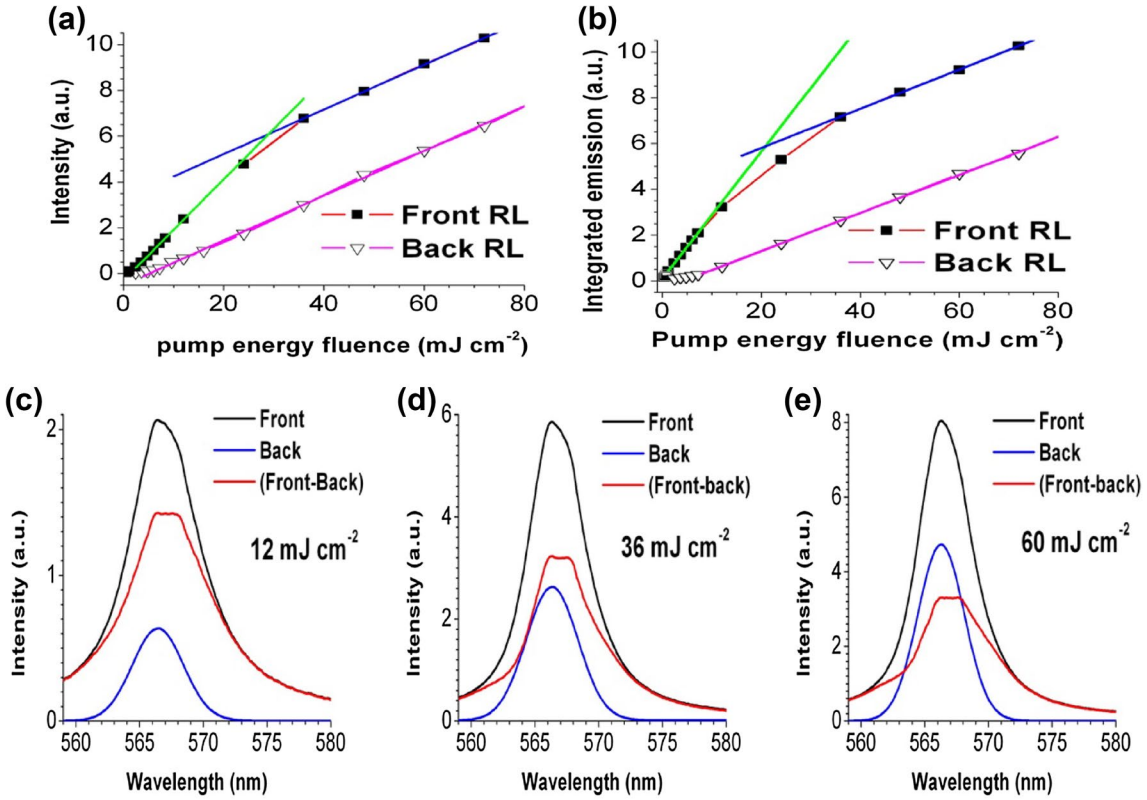

Fig. 10 Influence of the pump fluence on **a** emitted peak intensity for frontal and back collection, **b** is similar to **a** but is the spectrally integrated emission intensity. RL emission spectra by frontal and back collection for pumping fluencies of: **c** 12 mJ cm^{-2}, **d** 36 mJ cm^{-2} and **e** 60 mJ cm^{-2}. The back-collected spectra were rescaled, such that the intensity ratio (frontal/back collection) for each fluence would be the same found in Fig. 10a. The red solid lines represent the resulting spectra from the subtraction between frontal and back spectra (front-Back) (Color figure online)

a way for manufacturing random lasers with very low RL threshold.

3 Conclusions

In the first part of this work we detailed a strategy for increasing the efficiency of a random lasers that consists in using smaller particles, trapped between large particles to serve as absorption and gain centers whereas the large particles control mainly the light diffusion into the sample. The polydispersed samples demonstrated better laser performance with sample A4 showing the highest slope efficiency (51%) and optical to optical efficiency (34%). Threshold was 1.67 mJ and output power at the maximum absorbed pump power was 1.3 mJ. The slope efficiency is comparable to the best diode pumped Nd:YVO_4 solid state lasers, even when considering the more efficient longitudinal pumping configuration. For comparison, the best performing B group was B3 that demonstrated slope efficiency of 27% and optical-to-optical efficiency of 15%. However, for direct comparison A4 should be compared to B4 as shown in Fig. 5c. Group A4 has a more than three times higher output power than group B4, a lower threshold and stronger wavelength narrowing.

The results may be compared in the following way: light diffusion is the same in the monodispersed and polydispersed samples and governed by the larger particles whereas the smaller particles are responsible for an increase of local pump power density due to an increase of the density of scattering events of up to 15%. This proves that the strategy of separating and adjusting individually the effects of light diffusion and absorbed pump power density (and therefore gain) is a very promising technique to achieve evermore efficient random lasers.

On the other hand, core–shell TiO_2@Silica NPs at $[140 \times 10^{10}$ NPs $mL^{-1}]$ in an ethanol solution of R6G $[1 \times 10^{-4}$ M] allowed us to study the RL action at the localization transition. The FAP measurement provide an additional approach to the study of the scattering medium, which allows us to infer the RL threshold associated to localized modes. The back-collection method allowed for the separate measurement of the RL band mode, showing a linear dependence with pumping fluence without gain depletion. The emission spectrum of the peak modes was extracted by

subtracting the frontal and back spectra, showing a plateau in intensity in a broad frequency range. The latter suggests suppression of interaction between the peak modes, which is a signature of random lasing at localization. Localization of light besides being a fundamental topic, can open a way for manufacturing random lasers with a very low emission threshold.

References

1. V.S. Letokhov, Stimulated emission of an ensemble of scattering particles with negative absorption. JETP Lett. **5**, 212 (1967)
2. C. Gouedard, D. Husson, C. Sauteret, F. Auzel, A. Mingus, Generation of spatially incoherent short pulses in laser-pumped neodymium stoichiometric crystals and powders. J. Opt. Soc. Am. B **10**, 2358 (1993)
3. H. Cao, Y.G. Zhao, S.T. Ho, E.W. Seelig, Q.H. Wang, R.P.H. Chang, Random laser action in semiconductor powder. Phys. Rev. Lett. **82**, 2278 (1999)
4. R.C. Polson, A. Chipouline, Z.V. Vardeny, Random lasing in p-conjugated films and infiltrated opals. Adv. Mater. **13**, 760 (2001)
5. R.C. Polson, Z.V. Vardeny, Random lasing in human tissues. Appl. Phys. Lett. **85**, 1289 (2004)
6. E. Jimenez-Villar, V. Mestre, N.U. Wetter, G.F. de Sá, Core–shell (TiO_2@Silica) nanoparticles for random lasers. Proc. SPIE **10549**, 105490D (2018)
7. E. Jiménez-Villar, I.F. da Silva, V. Mestre, N.U. Wetter, C. Lopez, P.C. de Oliveira, W.M. Faustino, G.F. de Sá, Random lasing at localization transition in a colloidal suspension (TiO_2@Silica). ACS Omega **2**, 2415–2421 (2017)
8. Z. Wang, H. Wu, M. Fan, L. Zhang, Y. Rao, W. Zhang, X. Jia, High power random fiber laser with short cavity length: theoretical and experimental investigations. IEEE J. Sel. Top. Quantum Electron. **21**, 10 (2015)
9. H. Watanabe, Y. Oki, M. Maeda, T. Omatsu, Highly efficient long-lifetime dual-layered waveguide dye laser containing SiO_2 nanoparticle-dispersed random scattering active media. Appl. Phys. Lett. **86**, 151123 (2009)
10. K.C. Jorge, M.A. Alvarado, E.G. Melo, M.N.P. Carreño, M.I. Alayo, N.U. Wetter, Directional random laser source consisting of a HC-ARROW reservoir connected to channels for spectroscopic analysis in microfluidic devices. Appl. Opt. **55**, 5393 (2016)
11. S.K. Turitsyn et al., Random distributed feedback fibre laser. Nat. Photonics **4**, 231–235 (2010)
12. N.U. Wetter, E.C. Sousa, I.M. Ranieri, S.L. Baldochi, Compact, diode-side-pumped Nd^3:$YLiF_4$ laser at 1053 nm with 45% efficiency and diffraction- limited quality by mode controlling. Opt. Lett. **34**(3), 292 (2009). https://doi.org/10.1364/ol.34.000292
13. N.U. Wetter, F.A. Camargo, E.C. Sousa, Mode-controlling in a 7.5 cm long, transversally pumped, high power Nd:YVO_4 laser. J. Opt. A **10**(10), 104012 (2008). https://doi.org/10.1088/1464-4258/10/10/104012
14. N.U. Wetter, E.P. Maldonado, N.D. Vieira, Enhanced efficiency of a continuous-wave mode-locked Nd:YAG laser by compensation of the thermally induced, polarization-dependent bifocal lens. Appl. Opt. **32**(27), 5280 (1993). https://doi.org/10.1364/ao.32.005280
15. A. Bereczki, N.U. Wetter, 100 W continuous linearly polarized, high beam quality output from standard side-pumped Nd:YAG laser modules. Opt. Laser Technol. **96**, 271–275 (2017). https://doi.org/10.1016/j.optlastec.2017.05.020
16. A. Bereczki, M.A. Lopez, N.U. Wetter, Dynamically stable Nd:YAG resonators with beam quality beyond the birefringence limit and pumping of a singly resonant optical parametric oscillator. Opt. Lett. **43**(4), 695 (2018). https://doi.org/10.1364/ol.43.000695
17. N. Wetter, P.D. Matos, I. Ranieri, L. Courrol, S. Morato, Single frequency, continuously tunable, diode-pumped Nd:LiY0.5Gd0.5F4 microlaser. Opt. Commun. **204**(1–6), 311–315 (2002). https://doi.org/10.1016/s0030-4018(02)01237-3
18. N.U. Wetter, A.M. Deana, Power scaling of a side-pumped Nd:YLF laser based on DBMC technology. Appl. Phys. B **117**(3), 855–860 (2014). https://doi.org/10.1007/s00340-014-5897-8
19. N.U. Wetter, A.M. Deana, Influence of pump bandwidth on the efficiency of side-pumped, double-beam mode-controlled lasers: establishing a new record for Nd:YLiF_4 lasers using VBG. Opt. Express **23**(7), 9379 (2015). https://doi.org/10.1364/oe.23.009379
20. M.A. Noginov, I.N. Fowlkes, G. Zhu, Fiber-coupled random laser. Appl. Phys. Lett. **86**, 161105 (2005)
21. J. Azkargorta, I. Iparraguirre, M. Barredo-Zuriarrain, S. García-Revilla, R. Balda, J. Fernández, Random laser action in Nd:YAG crystal powder. Materials **9**, 369 (2016)
22. R.J. Vieira, L. Gomes, J.R. Martinelli, N.U. Wetter, Upconversion luminescence and decay kinetics in a diode-pumped nanocrystalline Nd^3:YVO_4 random laser. Opt. Express **20**(11), 12487 (2012). https://doi.org/10.1364/oe.20.012487
23. E. Jimenez-Villar, I.F. da Silva, V. Mestre, P.C. de Oliveira, W.M. Faustino, G.F. de Sá, Anderson localization of light in a colloidal suspension (TiO_2@silica). Nanoscale **8**(21), 10938–10946 (2016)
24. E. Jimenez Villar, V. Mestre, W.S. Martins, G.F. Basso, I.F. da Silva, G.F. de Sá, TiO_2@Silica nanoparticles for light confinement. Mater. Today Proc. **4**(11), 11570–11579 (2017)
25. E. Jimenez-Villar, M.C. S. Xavier, J.G.G.S. Ramos, N.U. Wetter, V. Mestre, W.S. Martins, G.F. Basso, V.A. Ermakov, F.C. Marques, Localization of light: beginning of a new optics. in D.L. Andrews, E.J. Galvez, J. Glückstad, eds *Complex Light and Optical Forces XII*. Proceeding SPIE p. 1054905
26. E. Jimenez-Villar, M.C.S. Xavier, N.U. Wetter, V. Mestre, W.S. Martins, G.F. Basso, V.A. Ermakov, F.C. Marques, G.F. de Sá, Photonics Res. **6**, 929 (2018)
27. P. Pradhan, N. Kumar, Localization of light in coherently amplifying random media. Phys. Rev. B **50**, 9644–9647 (1994)
28. R. Stano, P. Jacquod, Suppression of interactions in multimode random lasers in the Anderson localized regime. Nat. Photonics **7**, 66–71 (2013)
29. J. Liu et al., Random nanolasing in the Anderson localized regime. Nat. Nanotechnol. **9**, 285–289 (2014)
30. S. John, J. Wang, Quantum electrodynamics near a photonic band gap: photon bound states and dressed atoms. Phys. Rev. Lett. **64**, 2418–2421 (1990)
31. S. John, Localization of light. Phys. Today **44**, 32 (1991)
32. N.U. Wetter, J.M. Giehl, F. Butzbach, D. Anacleto, E. Jiménez-Villar, Polydispersed Powders (Nd3+:YVO 4) for ultra efficient random lasers. Syst. Charact. **35**, 1700335 (2017)
33. J.M. Giehl, A.R. Miranda, S.M. Reijn, F. Butzbach, N.U. Wetter. Relationship between coherent backscattering cone and the study of the random laser emission of Nd:YVO_4 powders changing the particle size and applied pressure. in *Advanced Solid-State Lasers (ASSL)*, 2014. Conference papers, 2014
34. N.U. Wetter, D.A.A. Da Silva, E. Jimenez-Villar, J.M. Giehl, Influence of the fraction of absorbed pump power on the performance of Nd^{3+}:YVO4 powder random lasers. in *Optical Components and Materials XV, 2018, San Francisco*. Optical Components and Materials XV, 2018. p. 68

35. K. Abderrafi, E. Jiménez, T. Ben, S.I. Molina, R. Ibáñez, V. Chirvony, J.P. Martínez-Pastor, Production of nanometer-size gaas nanocristals by nanosecond laser ablation in liquid. J. Nanosci. Nanotechnol. **12**(8), 6774–6778 (2012)
36. E. Jimenez-Villar, V. Mestre, P.C. de Oliveira, G.F. de Sá, Novel core–shell (TiO_2@Silica) nanoparticles for scattering medium in a random laser: higher efficiency, lower laser threshold and lower photodegradation. Nanoscale **5**(24), 12512 (2013)
37. E. Jimenez-Villar, V. Mestre, P.C. de Oliveira, W.M. Faustino, D.S. Silva, G.F. de Sá, TiO_2@Silica nanoparticles in a random laser: strong relationship of silica shell thickness on scattering medium properties and random laser performance. Appl. Phys. Lett. **104**(8), 081909 (2014)
38. E. Rodriguez, E. Jimenez, G.J. Jacob, A.A.R. Neves, C.L. Cesar, L.C. Barbosa, Fabrication and characterization of a PbTe quantum dots multilayer structure. Phys. E **26**(1–4), 361–365 (2005)
39. E. Rodriguez, G. Kellermann, A.F. Craievich, E. Jimenez, C.L. César, L.C. Barbosa, All-optical switching device for infrared based on PbTe quantum dots. Superlatt. Microstruct. **43**(5–6), 626–634 (2008)
40. E. Rodríguez, E. Jimenez, L.A. Padilha, A.A.R. Neves, G.J. Jacob, C.L. César, L.C. Barbosa, SiO2/PbTe quantum-dot multilayer production and characterization. Appl. Phys. Lett. **86**(11), 113117 (2005)
41. G. Kellermann, E. Rodriguez, E. Jimenez, C.L. Cesar, L.C. Barbosa, A.F. Craievich, Structure of PbTe(SiO 2)/SiO 2 multilayers deposited on Si(111). J. Appl. Crystallogr. **43**(3), 385–393 (2010)
42. E. Jiménez, K. Abderrafi, R. Abargues, J.L. Valdés, J.P. Martínez-Pastor, Laser-ablation-induced synthesis of SiO_2-capped noble metal nanoparticles in a single step. Langmuir **26**(10), 7458–7463 (2010)
43. E. Jiménez, K. Abderrafi, J. Martínez-Pastor, R. Abargues, J. Luís Valdés, R. Ibáñez, A novel method of nanocrystal fabrication based on laser ablation in liquid environment. Superlatt. Microstruct. **43**(5–6), 487–493 (2008)
44. J.R. González-Castillo, E. Rodriguez, E. Jimenez-Villar, D. Rodríguez, I. Salomon-García, G.F. de Sá, T. García-Fernández, D.B. Almeida, C.L. Cesar, R. Johnes, J.C. Ibarra, Synthesis of Ag@ Silica nanoparticles by assisted laser ablation. Nanoscale Res. Lett. **10**(1), 399 (2015)
45. J.R. González-Castillo, E. Rodríguez-González, E. Jiménez-Villar, C.L. Cesar, J.A. Andrade-Arvizu, Assisted laser ablation: silver/gold nanostructures coated with silica. Appl. Nanosci. **7**(8), 597–605 (2017)
46. G. Fuertes, O.L. Sánchez-Muñoz, E. Pedrueza, K. Abderrafi, J. Salgado, E. Jiménez, Switchable bactericidal effects from novel silica-coated silver nanoparticles mediated by light irradiation. Langmuir **27**(6), 2826–2833 (2011)
47. G. Fuertes, E. Pedrueza, K. Abderrafi, R. Abargues, O. Sánchez, J. Martínez-Pastor, J. Salgado, E. Jiménez, Photoswitchable bactericidal effects from novel silica-coated silver nanoparticles. ed. by R. Sroka and L. D. Lilge Prog. Biomed. Opt. Imaging—Proc. SPIE 8092, 80921M.
48. V.A. Ermakov, E. Jimenez-Villar, J.M.C. da Silva Filho, E. Yassitepe, N.V.V. Mogili, F. Iikawa, G.F. de Sá, C.L. Cesar, F.C. Marques, Size control of silver-core/silica-shell nanoparticles fabricated by laser-ablation-assisted chemical reduction. Langmuir **33**(9), 2257–2262 (2017)
49. O.L. Sánchez-Muñoz, J. Salgado, J. Martínez-Pastor, E. Jiménez-Villar, Synthesis and physical stability of novel Au–Ag@SiO_2 alloy nanoparticles. Nanosci. Nanotechnol. **2**(1), 1–7 (2012)
50. A.D. Mirlin, Statistics of energy levels and eigenfunctions in disordered systems. Phys. Rep. **326**, 259–382 (2000)
51. A.D. Mirlin, Spatial structure of anomalously localized states in disordered conductors. J. Math. Phys. **38**, 1888 (1997)
52. H. Cao et al., Spatial confinement of laser light in active random media. Phys. Rev. Lett. **84**, 5584 (2000)
53. G. Campagnano, YuV Nazarov, G_Q corrections in the circuit theory of quantum transport. Phys. Rev. B **74**, 125307 (2006)
54. A.L.R. Barbosa, D. Bazeia, J.G.G.S. Ramos, Universal Braess paradox in open quantum dots. Phys. Rev. E **90**, 042915 (2014)
55. X. Wu et al., Random lasing in closely packed resonant scatterers. J. Opt. Soc. Am. B **21**, 159–167 (2004)